Excitation functions of parameters in Erlang distribution, Schwinger mechanism, and Tsallis statistics in RHIC BES program

Li-Na Gao[a], Fu-Hu Liu[a,1], and Roy A. Lacey[b,2]
[a] *Institute of Theoretical Physics, Shanxi University, Taiyuan, Shanxi 030006, China*
[b] *Departments of Chemistry & Physics, Stony Brook University, Stony Brook, NY 11794, USA*

arXiv:1604.07218v1 [hep-ph] 25 Apr 2016

Abstract: Experimental results of the transverse momentum distributions of ϕ mesons and Ω hyperons produced in gold-gold (Au-Au) collisions with different centrality intervals, measured by the STAR Collaboration at different energies (7.7, 11.5, 19.6, 27, and 39 GeV) in the beam energy scan (BES) program at the relativistic heavy ion collider (RHIC), are approximately described by the single Erlang distribution and the two-component Schwinger mechanism. Meanwhile, the STAR experimental transverse momentum distributions of negatively charged particles, produced in Au-Au collisions at RHIC BES energies, are approximately described by the two-component Erlang distribution and the single Tsallis statistics. The excitation functions of free parameters are obtained from the fit to the experimental data. A weak softest point in the string tension in Ω hyperon spectra is observed at 7.7 GeV.

Keywords: Transverse momentum distribution, excitation functions of parameters, Erlang distribution, Schwinger mechanism, Tsallis statistics

PACS: 12.38.Mh, 25.75.Dw, 24.10.Pa

1 Introduction

High energy nucleus-nucleus (heavy ion) collisions at the relativistic heavy ion collider (RHIC) [1–3] and the large hadron collider (LHC) [4, 5] can provide the environment and condition of high temperature and density, where a new state of matter, namely the quark-gluon plasma (QGP), is expected to form [6–8]. Even at the top center-of-mass energy (the maximum $\sqrt{s_{NN}}$ = 19.4 GeV) of the super proton synchrotron (SPS), the equation of state (EoS) is possibly different from that at lower energy [9]. Both the RHIC and SPS have performed the beam energy scan (BES) programs, which give us opportunities to search for the onset of deconfinement of quarks and gluons, the critical point of phase transition from QGP to hadronic matter, and the softest points in the EoS in nucleus-nucleus collisions. The onset of quark deconfinement should be possibly the critical point of QGP phase transition. Although there is a relation between the softest points in the EoS and the critical point of QGP phase transition, they are not sure the same. In addition, different quantities result in different softest points, and the critical point should be exclusive. To reveal the relation between the softest points and critical point is still an open question.

Generally, the RHIC and its BES energies ($\sqrt{s_{NN}}$ = 7.7–200 GeV) [10–12] are larger than the SPS and its BES energies ($\sqrt{s_{NN}}$ = 6.6–19.4 GeV) [13–15], though they have an overlap each other. The STAR Collaboration has been performing the RHIC BES program [10–12], and the NA61/SHINE Collaboration has been performing the SPS BES program [13–15]. Some interesting results involved to the softest points in some excitation functions in the EoS have been reported. For example, the works which study excitation functions of ratio of positive kaon number to pions (K^+/π^+) [16–18], chemical freeze-out temperature (T_{ch}) [17, 18], mean transverse mass minus rest mass ($\langle m_T\rangle - m_0$) [17], and ratio of experimental negative pion rapidity (y) distribution width to Landau hydrodynamic model prediction [$\sigma_y(\pi^-)/\sigma_y$(hydro)] [18] show the softest point being around $\sqrt{s_{NN}}$ = 7–8 GeV. By using the Landau hydrodynamic model

[1]E-mail: fuhuliu@163.com; fuhuliu@sxu.edu.cn
[2]E-mail: Roy.Lacey@Stonybrook.edu

and the ultra-relativistic quantum molecular dynamics hybrid approach, an analysis based on rapidity distribution and squared speed-of-sound (c_s^2) extraction shows the softest point locating in the energy range from 4 to 9 GeV [19, 20].

Recently, a wiggle in the excitation function of a specific reduced curvature, C_y, of the net-proton rapidity distribution at midrapidity is expected in the energy range from 4 to 8 GeV [21, 22], where $C_y = (y_{\rm beam}^3 d^3N/dy^3)_{y=0}/(y_{\rm beam}dN/dy)_{y=0}$, $y_{\rm beam}$ denotes the beam rapidity, and N denotes the number of considered particles. A local weak wiggle in the C_y excitation function is exhibited in the range from 8 to 12 GeV. It is shown that there are more than one softest points in the EoS from 4 to 12 GeV. Our recent work which based on rapidity distribution and c_s^2 extraction shows the softest point being around 8.8 GeV [23], and there is a jump (from ≤ 0.3 to 1/3–1/2) in c_s^2 when the energy changes from 17.3 to 19.6 GeV. These phenomenons render that the interacting process is complex in the considered energy range. However, the searching for the onset of quark deconfinement and the critical point of QGP phase transition is not simple [24]. More analyses are needed in the study of the relation between the softest points and critical point.

The present work does not intend to reveal the relation between the softest points in the EoS and the critical points of QGP phase transition. Instead, we hope to search for more information of the softest points. In this paper, we study the transverse momentum spectra of different particles (ϕ mesons, Ω hyperons, and negatively charged particles) produced in gold-gold (Au-Au) collisions at a few RHIC BES energies (7.7, 11.5, 19.6, 27, and 39 GeV) by using the single (or two-component) Erlang distribution [25–27] for both hard and soft processes, two-component Schwinger mechanism [28–31] for hard process only, and single Tsallis statistics [32–34] for soft process only. The results calculated by the two methods (Schwinger and Erlang, or Tsallis and Erlang) are compared with the experimental data of the STAR Collaboration [35, 36].

The structure of the present work is as follows. The model and method are shortly described in section 2. Results and discussion are given in section 3. In section 4, we summarize our main observations and conclusions.

2 The model and method

Firstly, we discuss uniformly hard and soft collision processes in the framework of the multisource thermal model [25–27]. According to the model, a given particle is produced in the collision process where a few partons taken part in. Hard process contains two or three partons which are valence quarks. Soft process contains usually two or more partons which are gluons and sea quarks. Each (the i-th) parton is assumed to contribute to an exponential function [$f_i(p_t)$] of transverse momentum (p_t) distribution. Let $\langle p_t\rangle$ denotes the mean transverse momentum contributed by each (the i-th) parton, we have

$$f_i(p_t) = \frac{1}{\langle p_t\rangle}\exp\left(-\frac{p_t}{\langle p_t\rangle}\right). \tag{1}$$

The contribution of all n partons which taken part in the collision process is the folding of n exponential functions [25–27]. We have the transverse momentum (p_T) distribution $f(p_T)$ of final-state particles to be the Erlang distribution

$$f(p_T) = \frac{p_T^{n-1}}{(n-1)!\langle p_t\rangle^n}\exp\left(-\frac{p_T}{\langle p_t\rangle}\right), \tag{2}$$

which has the mean transverse momentum $\langle p_T\rangle = n\langle p_t\rangle$.

Secondly, the production of particles with heavy mass in hard process is also described by the Schwinger mechanism [28–31]. Let κ denote the string tension between partons which form a given final-state particle. Each (the i-th) parton has and then contributes to the given particle a Gaussian function of transverse momentum distribution

$$f_i(p_t) = \frac{1}{\sqrt{\kappa}}\exp\left(-\frac{\pi p_t^2}{\kappa}\right). \tag{3}$$

The transverse momentum distribution contributed by the string (two partons) is the folding of two

Gaussian functions. That is

$$f(p_T) = \int_0^{p_T} f_1(p_t) f_2(p_T - p_t) dp_t = \frac{1}{\kappa} \int_0^{p_T} \exp\left\{ - \frac{\pi[p_t^2 + (p_T - p_t)^2]}{\kappa} \right\} dp_t. \tag{4}$$

Thirdly, the Tsallis statistics which has more than one function forms [32–34] is also used to describe the thermal production of particles in soft process. We consider the simplest form of the Tsallis transverse momentum distribution at mid-rapidity

$$f(p_T) = C_T p_T \sqrt{p_T^2 + m_0^2} \left[1 + \frac{q-1}{T} \left(\sqrt{p_T^2 + m_0^2} - \mu \right) \right]^{-q/(q-1)}, \tag{5}$$

where T is the temperature which describes averagely a few local sources (equilibrium states), q is the entropy index which describes the degree of non-equilibrium among different local sources, μ is the chemical potential which is related to $\sqrt{s_{NN}}$ [37], m_0 is the rest mass of the considered particle, and C_T is the normalization constant which is related to other parameters.

In the Monte Carlo method, let r_i denote random numbers in [0,1]. The Erlang distribution results in

$$p_T = -\langle p_t \rangle \sum_{i=1}^{n} \ln r_i = -\langle p_t \rangle \ln \prod_{i=1}^{n} r_i. \tag{6}$$

Although both $-\langle p_t \rangle \sum_{i=1}^{n} \ln r_i$ and $-\langle p_t \rangle \ln \prod_{i=1}^{n} r_i$ can be used, we would rather use $-\langle p_t \rangle \sum_{i=1}^{n} \ln r_i$ than $-\langle p_t \rangle \ln \prod_{i=1}^{n} r_i$ due to $\prod_{i=1}^{n} r_i$ being probably a too small value for the calculation when n is large enough. Similarly, let $R_{1,2,3,4,5}$ denote random numbers in [0,1]. The Schwinger mechanism results in

$$p_T = \sqrt{\frac{\kappa}{\pi}} \left[\sqrt{-\ln R_1} \cos(2\pi R_2) + \sqrt{-\ln R_3} \cos(2\pi R_4) \right]. \tag{7}$$

The Tsallis distribution satisfies

$$\int_0^{p_T} f(p_T) dp_T < R_5 < \int_0^{p_T + dp_T} f(p_T) dp_T. \tag{8}$$

Sometimes, the experimental p_T distribution is the sum of two components with different weights. This means that we need the two-component function in some cases. Although we show the Monte Carlo method of the calculations, the analytical method is used in the present work, unless $(n-1)!$ is too large for the calculations.

It should be noted that the Erlang distribution shows flexible forms which are the foldings of two, three, $\cdots$, or multiple exponential functions, the Schwinger mechanism shows an inflexible form which is the folding of two Gaussian functions, while the Tsallis statistics shows relative flexible form which is the sum of two or three standard distributions [38]. The parameter $\langle p_t \rangle$ in the Erlang distribution renders the mean transverse momentum contributed by each parton, the parameter κ in the Schwinger mechanism renders the string tension between two collision partons, while the parameter T in the Tsallis statistics renders the excitation degree of interacting system. Because of the parton number in a string being fixed to two, the Schwinger mechanism is not suitable in analysis of soft process in which there are two or more partons, unless we consider multiple strings and the folding of multiple Gaussian functions in the process. In the case of using two or more components, the parameter value can be obtained by the average weighted those of different components. As a thermal description, the Tsallis statistics is not suitable in analysis of hard process in which heavy particles are produced by direct collisions between two or among three partons.

3 Results and discussion

Figure 1 presents the transverse momentum distributions, $d^2N/(2\pi N_{evt} p_T dy dp_T)$, of ϕ mesons produced in mid-rapidity ($|y| < 0.5$) in Au-Au collisions at five RHIC BES energies: (a) 7.7, (b) 11.5, (c) 19.6, (d) 27, and (e) 39 GeV, where N_{evt} denotes the event number and ϕ mesons are assumed to produce

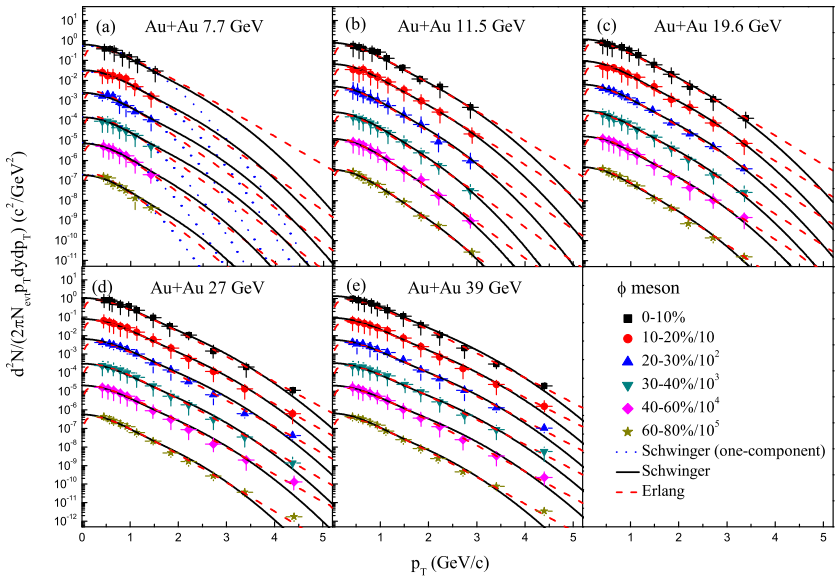

Figure 1. Transverse momentum distributions of ϕ mesons produced in $|y| < 0.5$ in Au-Au collisions at five RHIC BES energies: (a) 7.7, (b) 11.5, (c) 19.6, (d) 27, and (e) 39 GeV. The symbols represent the experimental data of the STAR Collaboration [35] in different centrality intervals, which are scaled by different amounts marked in the panel. The dashed and solid curves are our results calculated by using the single Erlang distribution and the two-component Schwinger mechanism respectively. The dotted curves in Figure 1(a) are an example calculated by using the single (one-component) Schwinger mechanism.

in hard process. The symbols represent the experimental data of the STAR Collaboration [35] in different centrality intervals, which are scaled by different amounts marked in the panel. The dashed and solid curves are our results calculated by using the single Erlang distribution and the two-component Schwinger mechanism respectively. The values of n for all the cases are taken to be 3. Other related parameter values are listed in Table 1 with values of χ^2 per degree of freedom (χ^2/dof), where k_{S1} denotes the relative contribution of the first component in the two-component Schwinger mechanism, and κ_1, κ_2, and $\langle p_t \rangle$, are the main free parameters in the two functions. One can see that both the single Erlang distribution and the two-component Schwinger mechanism describe approximately the experimental transverse momentum distributions of ϕ mesons produced in mid-rapidity in Au-Au collisions at the RHIC BES in most cases.

We would like to point out that the experimental data in narrow transverse momentum range should be described by the one-component formula of the Schwinger mechanism. As an example, the dotted curves in Figure 1(a) are the results of the single Schwinger mechanism with $\kappa = 1.462 \pm 0.283$, 1.435 ± 0.275, 1.300 ± 0.186, 1.156 ± 0.169, 1.070 ± 0.147, and 0.992 ± 0.163 GeV/fm, resulting in χ^2/dof=0.084, 0.123, 0.200, 0.056, 0.044, and 0.421, respectively, when the centrality interval changes from 0–10% to 60–80%. Although less parameters are used in the fit of one-component formula, it does not describe the data in wide transverse momentum range.

Figure 2 is similar to Figure 1, but it shows the results, $d^2N/(2\pi N_{evt} p_T dy dp_T)$, of Ω^- (solid symbols) and $\bar{\Omega}^+$ (open symbols divided by 2) in different centrality intervals, where the symbols represent the data of the STAR Collaboration [35] and Ω hyperons are assumed to produce in hard process. At the same time, the result of the one-component Schwinger mechanism is not available. The values of n for all the cases are taken to be 3. Other related parameters are listed in Table 2 with values of χ^2/dof. One can see that both the single Erlang distribution and the two-component Schwinger mechanism describe approximately the experimental data of Ω^- and $\bar{\Omega}^+$ produced in mid-rapidity region in Au-Au collisions at the RHIC BES in most cases.

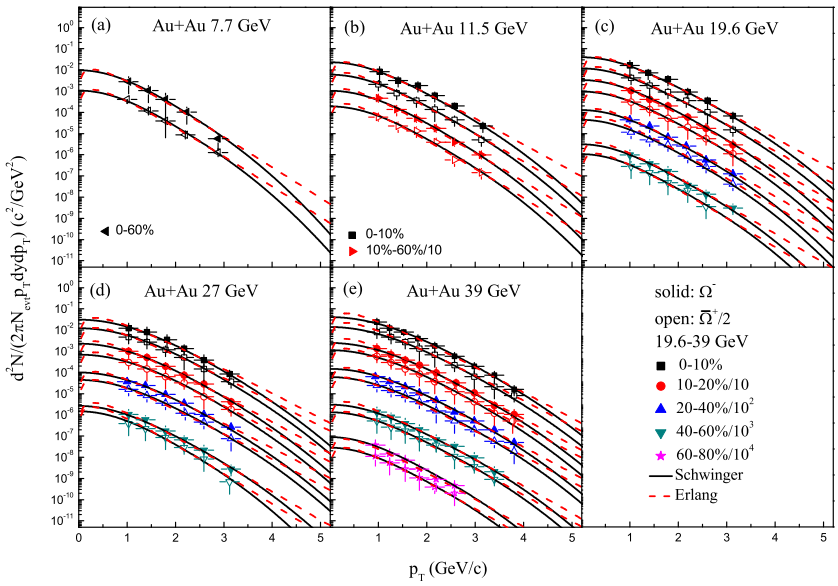

Figure 2. The same as for Fig. 1, but showing the results of Ω^- (solid symbols) and $\bar{\Omega}^+$ (open symbols divided by 2) in different centrality intervals, where the symbols represent the data of the STAR Collaboration [35]. At the same time, the results of the one-component Schwinger mechanism are not available.

Table 1. Values of parameters k_{S1}, κ_1, κ_2, and $\langle p_t \rangle$, as well as χ^2/dof corresponding to the solid and dashed curves in Fig. 1. In all the cases, for the single Erlang distribution, we have $n = 3$ which are not listed in the column.

		Two-component Schwinger mechanism				Single Erlang distribution	
Figure	Type	k_{S1}	κ_1 (GeV/fm)	κ_2 (GeV/fm)	χ^2/dof	$\langle p_t \rangle$ (GeV/c)	χ^2/dof
Figure 1(a)	0–10%	0.628 ± 0.135	0.967 ± 0.132	2.635 ± 0.245	0.050	0.287 ± 0.057	0.076
	10–20%	0.620 ± 0.133	0.952 ± 0.127	2.598 ± 0.228	0.120	0.247 ± 0.046	0.160
	20–30%	0.615 ± 0.137	0.936 ± 0.133	2.564 ± 0.237	0.225	0.231 ± 0.043	0.288
	30–40%	0.612 ± 0.132	0.895 ± 0.135	2.473 ± 0.238	0.066	0.230 ± 0.038	0.185
	40–60%	0.605 ± 0.128	0.862 ± 0.132	2.126 ± 0.219	0.066	0.228 ± 0.040	0.092
	60–80%	0.596 ± 0.133	0.787 ± 0.137	1.985 ± 0.225	0.364	0.208 ± 0.038	0.116
Figure 1(b)	0–10%	0.632 ± 0.132	0.988 ± 0.306	2.682 ± 0.382	0.269	0.273 ± 0.037	0.516
	10–20%	0.624 ± 0.124	0.953 ± 0.313	2.500 ± 0.375	0.096	0.267 ± 0.033	0.183
	20–30%	0.618 ± 0.108	0.922 ± 0.298	2.266 ± 0.323	0.113	0.247 ± 0.033	0.135
	30–40%	0.613 ± 0.115	0.892 ± 0.303	2.000 ± 0.337	0.020	0.238 ± 0.035	0.152
	40–60%	0.600 ± 0.113	0.870 ± 0.312	1.892 ± 0.357	0.063	0.228 ± 0.032	0.200
	60–80%	0.588 ± 0.122	0.823 ± 0.297	1.870 ± 0.345	0.214	0.218 ± 0.035	0.375
Figure 1(c)	0–10%	0.635 ± 0.157	1.092 ± 0.272	2.735 ± 0.336	0.112	0.278 ± 0.042	0.186
	10–20%	0.626 ± 0.148	0.976 ± 0.304	2.642 ± 0.358	0.115	0.273 ± 0.036	0.525
	20–30%	0.610 ± 0.153	0.952 ± 0.285	2.553 ± 0.326	0.129	0.262 ± 0.032	0.093
	30–40%	0.602 ± 0.155	0.938 ± 0.287	2.493 ± 0.347	0.132	0.260 ± 0.035	0.083
	40–60%	0.593 ± 0.157	0.923 ± 0.257	2.456 ± 0.334	0.967	0.258 ± 0.033	0.121
	60–80%	0.590 ± 0.152	0.832 ± 0.232	2.180 ± 0.305	0.364	0.242 ± 0.038	0.558
Figure 1(d)	0–10%	0.642 ± 0.162	1.238 ± 0.233	3.266 ± 0.256	0.703	0.290 ± 0.046	0.428
	10–20%	0.639 ± 0.177	1.182 ± 0.202	3.188 ± 0.233	0.422	0.286 ± 0.040	0.130
	20–30%	0.626 ± 0.172	1.128 ± 0.183	3.105 ± 0.225	1.278	0.282 ± 0.036	0.398
	30–40%	0.617 ± 0.168	1.080 ± 0.184	2.892 ± 0.217	0.475	0.275 ± 0.040	0.111
	40–60%	0.592 ± 0.176	0.993 ± 0.193	2.856 ± 0.206	1.493	0.275 ± 0.035	0.390
	60–80%	0.588 ± 0.188	0.870 ± 0.170	2.477 ± 0.200	9.734	0.258 ± 0.038	1.112
Figure 1(e)	0–10%	0.640 ± 0.186	1.278 ± 0.233	3.463 ± 0.313	0.685	0.300 ± 0.030	0.223
	10–20%	0.635 ± 0.182	1.182 ± 0.205	3.448 ± 0.322	0.427	0.308 ± 0.028	0.322
	20–30%	0.628 ± 0.173	1.160 ± 0.212	3.396 ± 0.302	1.151	0.300 ± 0.032	0.385
	30–40%	0.613 ± 0.178	1.129 ± 0.189	3.365 ± 0.295	0.756	0.298 ± 0.028	0.213
	40–60%	0.608 ± 0.180	1.098 ± 0.185	3.242 ± 0.290	0.398	0.285 ± 0.030	0.242
	60–80%	0.596 ± 0.177	0.905 ± 0.190	2.750 ± 0.293	4.921	0.277 ± 0.027	0.842

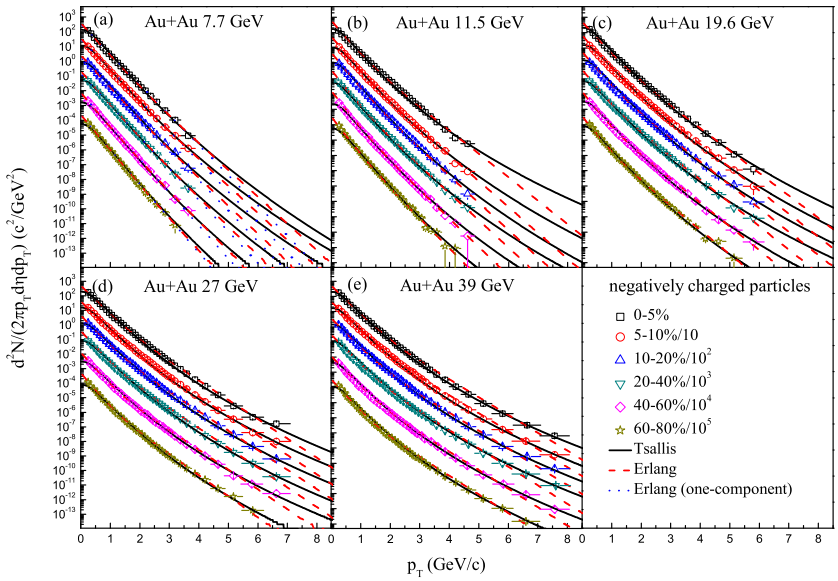

Figure 3. The same as for Fig. 1, but showing the results of negatively charged particles in $|\eta| < 0.5$ in different centrality intervals, where the symbols represent the data of the STAR Collaboration [36], and the dashed and solid curves are our results calculated by using the two-component Erlang distribution and the single Tsallis statistics respectively. The dotted curves in Figure 3(a) are an example calculated by using the one-component Erlang distribution.

Table 2. Values of parameters k_{S1}, κ_1, κ_2, and $\langle p_t \rangle$, as well as χ^2/dof corresponding to the solid and dashed curves in Fig. 2. In all the cases, for the single Erlang distribution, we have $n = 3$ which are not listed in the column.

		Two-component Schwinger mechanism				Single Erlang distribution	
Figure	Type	k_{S1}	κ_1 (GeV/fm)	κ_2 (GeV/fm)	χ^2/dof	$\langle p_t \rangle$ (GeV/c)	χ^2/dof
Figure 2(a)	0–60%	0.652 ± 0.118	1.564 ± 0.388	2.870 ± 0.298	0.145	0.280 ± 0.026	0.712
	0–60%	0.652 ± 0.103	1.580 ± 0.350	2.912 ± 0.303	0.270	0.282 ± 0.022	0.828
Figure 2(b)	0–10%	0.635 ± 0.115	1.788 ± 0.373	3.432 ± 0.305	0.304	0.321 ± 0.031	0.446
	0–10%	0.635 ± 0.103	1.782 ± 0.315	3.420 ± 0.300	0.104	0.302 ± 0.028	0.288
	10–60%	0.632 ± 0.126	1.753 ± 0.310	3.213 ± 0.288	0.209	0.293 ± 0.032	0.291
	10–60%	0.630 ± 0.118	1.732 ± 0.272	3.202 ± 0.282	0.329	0.288 ± 0.030	0.659
Figure 2(c)	0–10%	0.642 ± 0.120	1.852 ± 0.332	3.725 ± 0.332	0.124	0.325 ± 0.035	0.264
	0–10%	0.635 ± 0.117	1.786 ± 0.327	3.693 ± 0.318	0.134	0.315 ± 0.027	0.286
	10–20%	0.637 ± 0.122	1.715 ± 0.303	3.387 ± 0.302	0.042	0.303 ± 0.030	0.191
	10–20%	0.630 ± 0.118	1.706 ± 0.308	3.372 ± 0.307	0.037	0.310 ± 0.032	0.068
	20–40%	0.627 ± 0.124	1.658 ± 0.312	3.243 ± 0.297	0.109	0.306 ± 0.034	0.100
	20–40%	0.613 ± 0.113	1.643 ± 0.298	3.224 ± 0.290	0.186	0.300 ± 0.032	0.557
	40–60%	0.610 ± 0.124	1.543 ± 0.292	3.178 ± 0.288	0.091	0.296 ± 0.028	0.128
	40–60%	0.602 ± 0.118	1.482 ± 0.295	3.076 ± 0.284	0.121	0.290 ± 0.030	0.295
Figure 2(d)	0–10%	0.657 ± 0.108	2.420 ± 0.372	3.878 ± 0.382	0.049	0.343 ± 0.028	0.215
	0–10%	0.635 ± 0.102	2.395 ± 0.398	3.876 ± 0.400	0.035	0.349 ± 0.035	0.117
	10–20%	0.644 ± 0.111	2.246 ± 0.364	3.772 ± 0.362	0.041	0.326 ± 0.030	0.218
	10–20%	0.630 ± 0.114	2.356 ± 0.352	3.770 ± 0.380	0.054	0.332 ± 0.032	0.236
	20–40%	0.612 ± 0.103	2.176 ± 0.357	3.757 ± 0.337	0.097	0.340 ± 0.038	0.210
	20–40%	0.607 ± 0.100	2.030 ± 0.360	3.684 ± 0.364	0.026	0.330 ± 0.030	0.171
	40–60%	0.598 ± 0.123	1.843 ± 0.352	3.472 ± 0.353	0.133	0.302 ± 0.036	0.317
	40–60%	0.590 ± 0.102	1.662 ± 0.346	3.010 ± 0.230	0.179	0.282 ± 0.025	0.610
Figure 2(e)	0–10%	0.678 ± 0.120	2.564 ± 0.324	4.235 ± 0.325	0.066	0.331 ± 0.026	0.152
	0–10%	0.668 ± 0.124	2.478 ± 0.328	4.192 ± 0.302	0.128	0.335 ± 0.028	0.087
	10–20%	0.653 ± 0.115	2.346 ± 0.336	4.056 ± 0.316	0.061	0.328 ± 0.032	0.180
	10–20%	0.647 ± 0.117	2.260 ± 0.320	3.928 ± 0.318	0.199	0.333 ± 0.027	0.080
	20–40%	0.640 ± 0.108	2.232 ± 0.318	3.937 ± 0.303	0.220	0.330 ± 0.025	0.108
	20–40%	0.626 ± 0.117	2.030 ± 0.322	3.883 ± 0.322	0.077	0.332 ± 0.027	0.039
	40–60%	0.615 ± 0.121	1.856 ± 0.326	3.764 ± 0.315	0.074	0.315 ± 0.035	0.209
	40–60%	0.602 ± 0.126	1.802 ± 0.298	3.650 ± 0.308	0.047	0.318 ± 0.032	0.159
	60–80%	0.587 ± 0.127	1.588 ± 0.292	3.202 ± 0.313	0.266	0.305 ± 0.025	0.271
	60–80%	0.580 ± 0.118	1.526 ± 0.302	3.110 ± 0.310	0.118	0.302 ± 0.028	0.224

Table 3. Values of parameters T, q, k_{E1}, $\langle p_t\rangle_1$, and $\langle p_t\rangle_2$, as well as χ^2/dof corresponding to the solid and dashed curves in Fig. 3. In all the cases, for the two-component Erlang distribution, we have $n_1 = 3$ and $n_2 = 2$ which are not listed in the column.

		Single Tsallis statistics			Two-component Erlang distribution			
Figure	Type	T (GeV)	q	χ^2/dof	k_{E1}	$\langle p_t\rangle_1$ (GeV/c)	$\langle p_t\rangle_2$ (GeV/c)	χ^2/dof
Figure 3(a)	0–5%	0.152 ± 0.014	1.024 ± 0.008	1.442	0.821 ± 0.019	0.189 ± 0.013	0.240 ± 0.024	0.886
	5–10%	0.152 ± 0.012	1.026 ± 0.007	1.059	0.816 ± 0.021	0.187 ± 0.017	0.238 ± 0.026	2.648
	10–20%	0.151 ± 0.013	1.025 ± 0.008	1.924	0.812 ± 0.017	0.189 ± 0.014	0.232 ± 0.024	2.156
	20–40%	0.151 ± 0.015	1.022 ± 0.006	1.825	0.810 ± 0.017	0.183 ± 0.013	0.224 ± 0.020	0.860
	40–60%	0.150 ± 0.013	1.020 ± 0.008	1.487	0.807 ± 0.023	0.180 ± 0.010	0.220 ± 0.018	1.585
	60–80%	0.148 ± 0.010	1.018 ± 0.008	2.842	0.803 ± 0.020	0.176 ± 0.012	0.205 ± 0.020	1.634
Figure 3(b)	0–5%	0.150 ± 0.012	1.043 ± 0.006	5.003	0.826 ± 0.024	0.188 ± 0.016	0.285 ± 0.019	2.199
	5–10%	0.152 ± 0.014	1.034 ± 0.008	3.678	0.824 ± 0.027	0.178 ± 0.013	0.258 ± 0.022	1.657
	10–20%	0.150 ± 0.011	1.031 ± 0.008	4.948	0.817 ± 0.026	0.178 ± 0.015	0.246 ± 0.018	4.594
	20–40%	0.150 ± 0.012	1.033 ± 0.005	2.410	0.795 ± 0.022	0.173 ± 0.011	0.245 ± 0.013	2.956
	40–60%	0.150 ± 0.014	1.030 ± 0.007	2.983	0.786 ± 0.024	0.168 ± 0.015	0.234 ± 0.017	2.460
	60–80%	0.148 ± 0.008	1.027 ± 0.008	4.885	0.773 ± 0.023	0.163 ± 0.013	0.225 ± 0.016	4.242
Figure 3(c)	0–5%	0.152 ± 0.010	1.038 ± 0.010	4.495	0.835 ± 0.027	0.196 ± 0.018	0.297 ± 0.023	1.840
	5–10%	0.156 ± 0.012	1.035 ± 0.006	5.609	0.826 ± 0.023	0.187 ± 0.013	0.288 ± 0.017	1.180
	10–20%	0.153 ± 0.010	1.036 ± 0.007	8.570	0.819 ± 0.025	0.183 ± 0.016	0.285 ± 0.019	2.184
	20–40%	0.153 ± 0.008	1.039 ± 0.006	3.641	0.808 ± 0.018	0.178 ± 0.020	0.285 ± 0.023	3.866
	40–60%	0.151 ± 0.013	1.037 ± 0.008	3.354	0.795 ± 0.022	0.173 ± 0.014	0.280 ± 0.018	3.457
	60–80%	0.150 ± 0.011	1.034 ± 0.006	5.860	0.793 ± 0.024	0.168 ± 0.017	0.272 ± 0.020	2.821
Figure 3(d)	0–5%	0.152 ± 0.012	1.043 ± 0.006	7.770	0.875 ± 0.032	0.213 ± 0.018	0.328 ± 0.028	3.921
	5–10%	0.154 ± 0.014	1.043 ± 0.008	6.243	0.870 ± 0.028	0.206 ± 0.015	0.326 ± 0.024	3.135
	10–20%	0.154 ± 0.011	1.042 ± 0.007	5.889	0.866 ± 0.026	0.200 ± 0.022	0.325 ± 0.025	2.309
	20–40%	0.155 ± 0.012	1.042 ± 0.006	3.860	0.862 ± 0.030	0.192 ± 0.017	0.320 ± 0.027	8.382
	40–60%	0.155 ± 0.013	1.043 ± 0.010	3.818	0.858 ± 0.030	0.185 ± 0.017	0.320 ± 0.024	4.309
	60–80%	0.148 ± 0.012	1.040 ± 0.007	5.483	0.853 ± 0.027	0.178 ± 0.013	0.300 ± 0.022	5.546
Figure 3(e)	0–5%	0.150 ± 0.013	1.050 ± 0.007	3.193	0.920 ± 0.035	0.226 ± 0.020	0.370 ± 0.024	6.894
	5–10%	0.152 ± 0.014	1.048 ± 0.006	4.982	0.913 ± 0.027	0.223 ± 0.017	0.368 ± 0.027	3.643
	10–20%	0.153 ± 0.012	1.048 ± 0.007	4.178	0.910 ± 0.032	0.218 ± 0.015	0.365 ± 0.022	5.659
	20–40%	0.153 ± 0.014	1.049 ± 0.009	9.191	0.908 ± 0.026	0.216 ± 0.017	0.358 ± 0.025	9.063
	40–60%	0.151 ± 0.012	1.049 ± 0.006	6.714	0.902 ± 0.028	0.210 ± 0.014	0.356 ± 0.023	6.465
	60–80%	0.150 ± 0.014	1.049 ± 0.008	4.322	0.895 ± 0.025	0.200 ± 0.015	0.352 ± 0.024	6.094

To give a comparison, Figure 3 gives the results, $d^2N/(2\pi p_T d\eta dp_T)$, of negatively charged particles (hadrons) (h^-) produced in mid-pseudorapidity ($|\eta| < 0.5$) in the same collisions with a bit difference in centrality intervals, where h^- are assumed to produce mostly in soft process and the contribution of hard process to h^- with high p_T is neglected due to small amount. The symbols represent the data of the STAR Collaboration [36], and the dashed and solid curves are our results calculated by using the two-component Erlang distribution and the single Tsallis statistics respectively. The dotted curves in Figure 3(a) are the results of single Erlang distribution, which are given as an example and are not in agreement with the spectra in wide transverse momentum range. The values of n_1 and n_2 for all the cases are taken to be 3 and 2 respectively. Other related parameter values related to the two-component Erlang distribution and the single Tsallis statistics are listed in Table 3 with values of χ^2/dof. The chemical potentials related to collision energy [37] in Eq. (5) are taken to be 0.407, 0.304, 0.197, 0.149, and 0.107 GeV which correspond to 7.7, 11.5, 19.6, 27, and 39 GeV, respectively. For the dotted curves in Figure 3(a) and the centralities from 0–5% to 60–80%, the values of $\langle p_t\rangle$ in the single Erlang distribution are taken to be 0.212 ± 0.025, 0.210 ± 0.023, 0.209 ± 0.022, 0.203 ± 0.018, 0.194 ± 0.021, and 0.186 ± 0.022 GeV/c, and the values of n for all the six cases are taken to be 3, which result in the values of χ^2/dof to be 0.922, 2.430, 1.980, 0.930, 1.374, and 1.965, respectively. One can see that the two-component Erlang distribution and the single Tsallis statistics describe approximately the experimental data of h^- produced in mid-pseudorapidity in Au-Au collisions at the RHIC BES in most cases.

To study the change trends of parameters with centrality interval (C) and collision energy ($\sqrt{s_{NN}}$), Figure 4 shows the dependences of parameters k_{S1}, κ_1, κ_2, and $\langle p_t\rangle$ on centrality at different energies (left panel) and on energy in different centrality intervals (right panel). The different symbols represent the parameter values extracted from Figure 1 and listed in Table 1, where the two-component Schwinger mechanism and single Erlang distribution are used for ϕ spectra. The lines are our fitted results, and the values of intercepts, slopes, and χ^2/dof are listed in Table 4. Figure 5 is the same as that for Figure 4, but it shows the parameter values extracted from Figure 2 and listed in Table 2, where the two-component Schwinger mechanism and single Erlang distribution are used for Ω^- (solid symbols) and $\bar{\Omega}^+$ (open symbols) spectra respectively. In particular, the solid and open symbols in Figure 5 are shifted respectively to the left and right sides by a small amount for clearness. The values of intercepts, slopes, and χ^2/dof corresponding to the lines in Figure 5 are listed in Table 5. Figure 6 displays the dependences of parameters T, q, k_{E1}, $\langle p_t\rangle_1$, and $\langle p_t\rangle_2$ on centrality at different energies (left panel) and on energy in different centrality intervals (right panel). The different symbols represent the parameter values extracted from Figure 3 and listed in Table 3, where the single Tsallis statistics and two-component Erlang distribution are used for negatively charged particle spectra. The values of intercepts, slopes, and χ^2/dof corresponding to the lines in Figure 6 are listed in Table 6.

One can see from Figures 4–6 that the relative contribution of the first component in the two-component Schwinger mechanism decreases slightly with decrease of centrality, and does not show an obvious change with

change of collision energy [Figures 4(a), 4(b), 5(a), and 5(b)]. The relative contribution of the first component in the two-component Erlang distribution decreases slightly with decrease of centrality, and increases with increase of collision energy [Figures 6(e) and 6(f)]. The mean transverse momentum contributed by each parton in the Erlang distribution decrease with decrease of centrality [Figures 4(g), 5(g), 6(g), and 6(i)], and increase with increase of collision energy [Figures 4(h), 5(h), 6(h), and 6(j)]. The string tension between partons in the Schwinger mechanism decrease also with decrease of centrality [Figures 4(c), 4(e), 5(c), and 5(e)], and increase also with increase of collision energy [Figures 4(d), 4(f), 5(d), and 5(f)]. The effective temperature of emission source in the Tsallis statistics does not show an obvious dependence on centrality and collision energy [Figure 6(a) and 6(b)]. The entropy index does not show an obvious change with change of centrality, and increase with increase of collision energy [Figures 6(c) and 6(d)]. A weak softest point in the string tension in Ω hyperon spectra is observed at 7.7 GeV [Figures 5(e) and 5(g)].

To study the relations between different distributions, as well as their parameters, we could give some further discussions. It should be noted that Figures 1 and 2 devoted to multi-strange hadrons $\phi(s\bar{s})$ mesons and $\Omega(sss)$ hyperons respectively. Both $\phi(s\bar{s})$ mesons and $\Omega(sss)$ hyperons are expected to have relatively small hadronic interaction cross-sections. They are also important probes for the search of the QGP phase transition [35]. We have used the two-component Schwinger mechanism and the single Erlang distribution to describe the spectra of multi-strange hadrons which are expected to be produced in hard scattering process. Although the Schwinger mechanism can give the string tension κ between partons, the flexible Erlang distribution can describe the violent degree of parton-parton interactions or excitation degree of interacting system (emission source) by the mean transverse momentum $\langle p_t \rangle$ contributed by each parton and the mean transverse momentum $\langle p_T \rangle$ contributed by n partons. From the comparisons between the Schwinger mechanism and Erlang distribution in Figure 1 and Table 1, we can obtain the linear relations between κ and $\langle p_T \rangle$ for ϕ mesons in Figures 7(a) and 7(b) which correspond respectively to different energies (in various centrality intervals) and to different centrality intervals (at various energies). Similarly, the results for Ω (Ω^- and $\bar{\Omega}^+$) hyperons are presented in Figures 7(c) and 7(d) based on Figure 2 and Table 2. Different symbols represent different energies and centrality intervals, where C_1, C_2, $\cdots$, C_6 for Figures 7(b) and 7(d) represent respectively and successively the centrality intervals mentioned in the right panels of Figures 4 and 5, and the lines are our fitted results. The values of intercepts, slopes, and χ^2/dof are listed in Table 7. One can see that κ increases with increase of $\langle p_T \rangle$. There is a one-to-one correspondence between the two-component Schwinger mechanism and the single Erlang distribution.

For the spectra of negatively charged hadrons presented in Figure 3, we have used the single Tsallis statistics and the two-component Erlang distribution. Because of the Tsallis statistics resulting in the sum of two or three standard distribution [38], it has the temperature parameter T which describes the excitation degree of interacting system. The mean transverse momentum $\langle p_T \rangle$ obtained from the two-component Erlang distribution also describes the excitation degree of interacting system. From the comparisons between the single Tsallis statistics and the two-component Erlang distribution in Figure 3 and Table 3, we can obtain the linear relations between T and $\langle p_T \rangle$ in Figures 7(e) and 7(f) which correspond respectively to different collision energies (in various centrality intervals) and to different centrality intervals (at various energies), where C_1, C_2, $\cdots$, C_6 for Figure 7(f) represent successively the centrality intervals mentioned in the right panel of Figure 6. The values of intercepts, slopes, and χ^2/dof are listed in Table 7. One can see that T does not show an obvious change with increase of $\langle p_T \rangle$. Instead, Figure 6 shows that q and $\langle p_T \rangle$ increase with increase of $\sqrt{s_{NN}}$, which renders that q increases with increase of $\langle p_T \rangle$. There is a one-to-one correspondence between the single Tsallis statistics and the two-component Erlang distribution. Because the Schwinger mechanism and Tsallis statistics do not describe the same set of experimental data. We do not expect to study the relation between κ and T. In addition, in the case of considering the two-component functions, we obtain the values of κ, T, and $\langle p_T \rangle$ discussed above to be respectively an average weighted by the two components.

In our recent works [39, 40], we have studied the two-component Schwinger mechanism and the two-component Erlang distribution for J/ψ and Υ productions [39], and Lévy distribution and the multi-component Erlang distribution for identified particles productions [40]. In most cases, different functions (Schwinger and Eralng or Tsallis and Erlang) describe the same set of experimental data (hard or soft particles), which reflects the relations among them. The relations between κ and $\langle p_T \rangle$, as well as T and $\langle p_T \rangle$, discussed above are an attempt to study these relations. In particular, the single and two-component Erlang distributions describe the particle spectra in hard and soft processes respectively, which reflects the Erlang distribution being flexible. We think that there are some universal laws existing in the two processes. If the hard process corresponds to a violent collision, the soft process corresponds to a non-violent or a very non-violent collision. Only from the collision itself, both the hard and soft processes obey the same Erlang distribution with different $\langle p_t \rangle$ and parton numbers. We think that the Erlang distribution is one of the universal laws existing in the hard and soft processes.

4 Conclusions

We summarize here our main observations and conclusions.

a) The transverse momentum distributions of ϕ mesons, Ω hyperons, and negatively charged particles produced in mid-(pseudo)rapidity in Au-Au collisions with different centrality intervals at RHIC BES energies are analyzed by using the single or two-component Erlang distribution, the two-component Schwinger mechanism, and the single Tsallis statistics. The single or two-component Erlang distribution is approximately in agreement with the experimental data measured by the STAR Collaboration over an energy range from 7.7 to 39 GeV. The two-component Schwinger mechanism describes approximately the data of ϕ mesons and Ω hyperons which are

assumed to produce in hard process. The single Tsallis statistics describes approximately the data of negatively charged particles in which most are assumed to produce in soft process.

b) The mean transverse momentum contributed by each parton in the Erlang distribution which describes ϕ mesons, Ω hypersons, and negatively charged particles, and the string tension between partons in the Schwinger mechanism which describes ϕ mesons and Ω hypersons, decrease with decrease of centrality, and increase with increase of collision energy. The effective temperature of emission source in the Tsallis statistics which describes the negatively charged particles does not show an obvious dependence on centrality and collision energy. The entropy index does not show an obvious change with change of centrality, and increase with increase of collision energy. A weak softest point in the string tension in Ω hyperon spectra is observed at 7.7 GeV.

c) The relative contribution of the first component in the two-component Erlang distribution which describes the negatively charged particles decreases slightly with decrease of centrality, and increases with increase of collision energy. The relative contribution of the first component in the two-component Schwinger mechanism which describes ϕ mesons and Ω hypersons decreases slightly with decrease of centrality, and does not show an obvious change with change of collision energy.

d) In the descriptions of hard process, the string tension in the two-component Schwinger mechanism increases with increase of the mean transverse momentum in the single Erlang distribution. There is a one-to-one correspondence between the two descriptions for hard process. In the descriptions of soft process, the temperature and entropy index in the single Tsallis statistics unchanges approximately or increases with increase of mean transverse momentum in the two-component Erlang distribution. There is also a one-to-one correspondence between the two descriptions for soft process.

Conflict of interests

The authors declare that there is no conflict of interests regarding the publication of this paper.

Acknowledgments

This work was supported by the National Natural Science Foundation of China under Grant No. 11575103 and the US DOE under contract DE-FG02-87ER40331.A008.

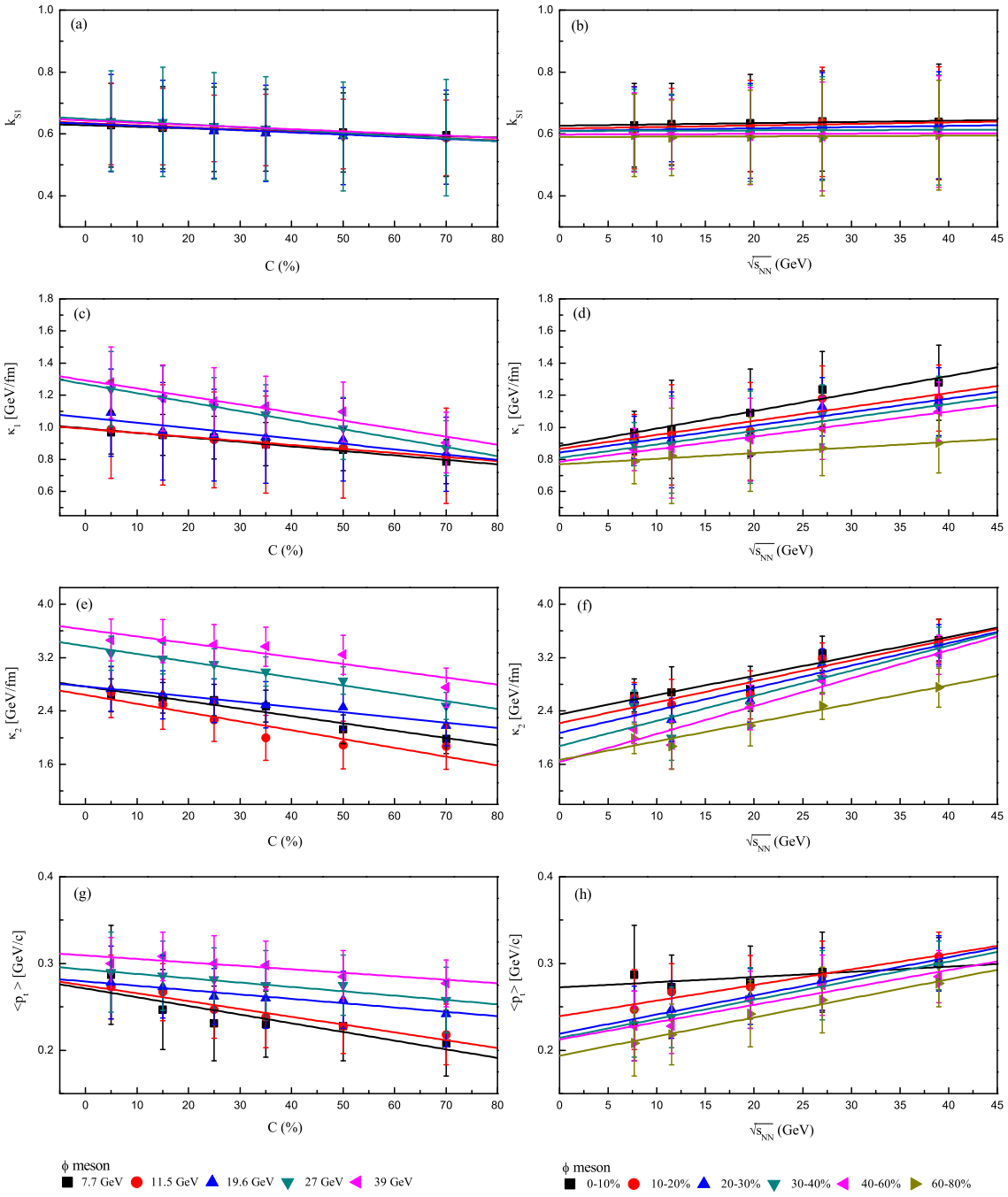

Figure 4. Dependences of parameters (a,b) k_{S1}, (c,d) κ_1, (e,f) κ_2, and (g,h) $\langle p_t \rangle$ on centrality at different energies (left panel) and on energy in different centrality intervals (right panel). The different symbols represent the parameter values extracted from Fig. 1 and listed in Table 1, where the two-component Schwinger mechanism and single Erlang distribution are used for ϕ spectra. The lines are our fitted results.

Table 4. Values of intercepts, slopes, and χ^2/dof corresponding to the lines in Fig. 4 which shows dependences of parameters on centrality at different energies (a,c,e,g) and on energy in different centrality intervals (b,d,f,h). The values of parameters are extracted from Fig. 1 and listed in Table 1.

Figure	Relation	Type	Intercept	Slope	χ^2/dof
			Two-component Schwinger mechanism in Fig. 1		
Figure 4(a)	$k_{S1} - C$	7.7 GeV	0.628 ± 0.001	-0.00047 ± 0.00002	0.001
		11.5 GeV	0.635 ± 0.001	-0.00067 ± 0.00002	0.001
		19.6 GeV	0.633 ± 0.004	-0.00072 ± 0.00011	0.002
		27 GeV	0.649 ± 0.004	-0.00094 ± 0.00010	0.001
		39 GeV	0.644 ± 0.001	-0.00070 ± 0.00006	0.001
Figure 4(b)	$k_{S1} - \sqrt{s_{NN}}$	0–10%	0.627 ± 0.002	0.00040 ± 0.00011	0.001
		10–20%	0.618 ± 0.004	0.00054 ± 0.00016	0.001
		20–30%	0.610 ± 0.005	0.00044 ± 0.00020	0.002
		30–40%	0.610 ± 0.005	0.00008 ± 0.00022	0.002
		40–60%	0.598 ± 0.007	0.00006 ± 0.00028	0.003
		60–80%	0.590 ± 0.004	0.00006 ± 0.00016	0.001
Figure 4(c)	$\kappa_1 - C$	7.7 GeV	0.993 ± 0.007	-0.00280 ± 0.00019	0.007
		11.5 GeV	0.990 ± 0.006	-0.00246 ± 0.00015	0.001
		19.6 GeV	1.062 ± 0.024	-0.00329 ± 0.00059	0.020
		27 GeV	1.269 ± 0.004	-0.00561 ± 0.00010	0.001
		39 GeV	1.292 ± 0.026	-0.00500 ± 0.00065	0.042
Figure 4(d)	$\kappa_1 - \sqrt{s_{NN}}$	0–10%	0.883 ± 0.034	0.01093 ± 0.00141	0.030
		10–20%	0.866 ± 0.050	0.00874 ± 0.00212	0.079
		20–30%	0.843 ± 0.042	0.00844 ± 0.00175	0.063
		30–40%	0.810 ± 0.030	0.00844 ± 0.00124	0.032
		40–60%	0.786 ± 0.012	0.00777 ± 0.00049	0.007
		60–80%	0.769 ± 0.009	0.00354 ± 0.00037	0.003
Figure 4(e)	$\kappa_2 - C$	7.7 GeV	2.640 ± 0.095	-0.01105 ± 0.00140	0.127
		11.5 GeV	2.771 ± 0.030	-0.01316 ± 0.00238	0.165
		19.6 GeV	3.374 ± 0.040	-0.00783 ± 0.00077	0.020
		27 GeV	3.620 ± 0.085	-0.01180 ± 0.00101	0.080
		39 GeV	2.765 ± 0.056	-0.01029 ± 0.00214	0.185
Figure 4(f)	$\kappa_2 - \sqrt{s_{NN}}$	0–10%	2.351 ± 0.112	0.02887 ± 0.00469	0.213
		10–20%	2.217 ± 0.132	0.03142 ± 0.00553	0.326
		20–30%	2.073 ± 0.177	0.03357 ± 0.00743	0.643
		30–40%	1.876 ± 0.220	0.03763 ± 0.00924	0.948
		40–60%	1.638 ± 0.140	0.04182 ± 0.00590	0.391
		60–80%	1.666 ± 0.081	0.02797 ± 0.00339	0.140
			Single Erlang distribution in Fig. 1		
Figure 4(g)	$\langle p_t \rangle - C$	7.7 GeV	0.271 ± 0.010	-0.00098 ± 0.00025	0.095
		11.5 GeV	0.275 ± 0.004	-0.00088 ± 0.00010	0.029
		19.6 GeV	0.279 ± 0.002	-0.00051 ± 0.00006	0.011
		27 GeV	0.293 ± 0.002	-0.00046 ± 0.00005	0.007
		39 GeV	0.309 ± 0.003	-0.00044 ± 0.00009	0.031
Figure 4(h)	$\langle p_t \rangle - \sqrt{s_{NN}}$	0–10%	0.272 ± 0.007	0.00063 ± 0.00028	0.032
		10–20%	0.239 ± 0.004	0.00177 ± 0.00019	0.023
		20–30%	0.219 ± 0.004	0.00216 ± 0.00016	0.016
		30–40%	0.214 ± 0.002	0.00220 ± 0.00008	0.005
		40–60%	0.212 ± 0.007	0.00202 ± 0.00028	0.062
		60–80%	0.194 ± 0.004	0.00223 ± 0.00016	0.018

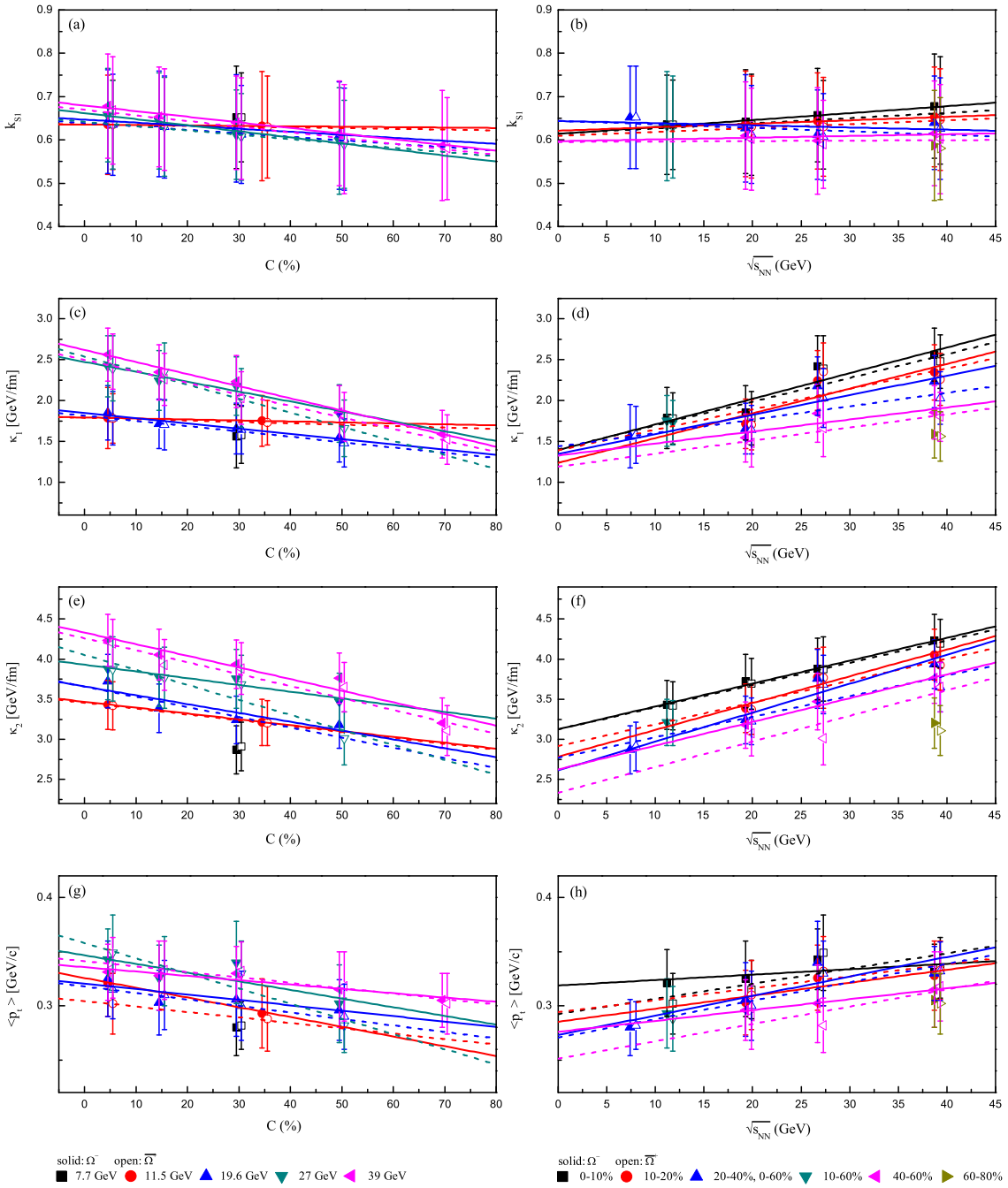

Figure 5. As for Fig. 4, but showing the parameter values extracted from Fig. 2 and listed in Table 2, where the two-component Schwinger mechanism and single Erlang distribution are used for Ω^- (solid symbols) and $\bar{\Omega}^+$ (open symbols) spectra respectively. The solid and open symbols are shifted respectively to the left and right sides by a small amount for clearness.

Table 5. Values of intercepts, slopes, and χ^2/dof corresponding to the lines in Fig. 5 which shows dependences of parameters on centrality at different energies (a,c,e,g) and on energy in different centrality intervals (b,d,f,h). The values of parameters are extracted from Fig. 2 and listed in Table 2.

Figure	Relation	Type	Intercept	Slope	χ^2/dof
			Two-component Schwinger mechanism in Fig. 2		
Figure 5(a)	$k_{S1} - C$	11.5 GeV Ω^-	0.636 ± 0.000	-0.00009 ± 0.00000	0.001
		11.5 GeV $\bar{\Omega}^+$	0.636 ± 0.000	-0.00017 ± 0.00000	0.001
		19.6 GeV Ω^-	0.647 ± 0.001	-0.00072 ± 0.00004	0.001
		19.6 GeV $\bar{\Omega}^+$	0.639 ± 0.002	-0.00077 ± 0.00007	0.001
		27 GeV Ω^-	0.662 ± 0.005	-0.00136 ± 0.00017	0.005
		27 GeV $\bar{\Omega}^+$	0.642 ± 0.003	-0.00106 ± 0.00009	0.001
		39 GeV Ω^-	0.680 ± 0.003	-0.00132 ± 0.00008	0.002
		39 GeV $\bar{\Omega}^+$	0.670 ± 0.003	-0.00132 ± 0.00007	0.001
Figure 5(b)	$k_{S1} - \sqrt{s_{NN}}$	0–10% Ω^-	0.614 ± 0.003	0.00161 ± 0.00013	0.001
		0–10% $\bar{\Omega}^+$	0.614 ± 0.012	0.00119 ± 0.00044	0.011
		10–20% Ω^-	0.621 ± 0.001	0.00082 ± 0.00004	0.001
		10–20% $\bar{\Omega}^+$	0.609 ± 0.008	0.00093 ± 0.00027	0.002
		20–40% Ω^-	0.644 ± 0.018	-0.00047 ± 0.00071	0.033
		20–40% $\bar{\Omega}^+$	0.644 ± 0.019	-0.00083 ± 0.00074	0.034
		40–60% Ω^-	0.597 ± 0.017	0.00037 ± 0.00057	0.008
		40–60% $\bar{\Omega}^+$	0.595 ± 0.015	0.00010 ± 0.00050	0.008
Figure 5(c)	$\kappa_1 - C$	11.5 GeV Ω^-	1.794 ± 0.000	-0.00117 ± 0.00000	0.001
		11.5 GeV $\bar{\Omega}^+$	1.790 ± 0.000	-0.00167 ± 0.00000	0.001
		19.6 GeV Ω^-	1.851 ± 0.027	-0.00637 ± 0.00090	0.014
		19.6 GeV $\bar{\Omega}^+$	1.818 ± 0.014	-0.00653 ± 0.00046	0.004
		27 GeV Ω^-	2.474 ± 0.043	-0.01209 ± 0.00144	0.028
		27 GeV $\bar{\Omega}^+$	2.540 ± 0.050	-0.01718 ± 0.00164	0.034
		39 GeV Ω^-	2.620 ± 0.032	-0.01480 ± 0.00078	0.021
		39 GeV $\bar{\Omega}^+$	2.500 ± 0.029	-0.01414 ± 0.00071	0.017
Figure 5(d)	$\kappa_1 - \sqrt{s_{NN}}$	0–10% Ω^-	1.394 ± 0.185	0.03140 ± 0.00702	0.245
		0–10% $\bar{\Omega}^+$	1.404 ± 0.216	0.02907 ± 0.00823	0.326
		10–20% Ω^-	1.240 ± 0.355	0.03020 ± 0.01200	0.469
		10–20% $\bar{\Omega}^+$	1.393 ± 0.537	0.02505 ± 0.01812	1.115
		20–40% Ω^-	1.350 ± 0.164	0.02392 ± 0.00631	0.276
		20–40% $\bar{\Omega}^+$	1.439 ± 0.129	0.01638 ± 0.00497	0.174
		40–60% Ω^-	1.328 ± 0.221	0.01470 ± 0.00746	0.194
		40–60% $\bar{\Omega}^+$	1.191 ± 0.071	0.01603 ± 0.00240	0.021
Figure 5(e)	$\kappa_2 - C$	11.5 GeV Ω^-	3.468 ± 0.000	-0.00730 ± 0.00000	0.001
		11.5 GeV $\bar{\Omega}^+$	3.456 ± 0.000	-0.00727 ± 0.00000	0.001
		19.6 GeV Ω^-	3.659 ± 0.027	-0.01105 ± 0.00333	0.200
		19.6 GeV $\bar{\Omega}^+$	3.658 ± 0.014	-0.01266 ± 0.00266	0.130
		27 GeV Ω^-	3.930 ± 0.043	-0.00843 ± 0.00160	0.033
		27 GeV $\bar{\Omega}^+$	4.054 ± 0.012	-0.01874 ± 0.00401	0.214
		39 GeV Ω^-	4.331 ± 0.082	-0.01449 ± 0.00198	0.147
		39 GeV $\bar{\Omega}^+$	4.260 ± 0.085	-0.01494 ± 0.00204	0.158
Figure 5(f)	$\kappa_2 - \sqrt{s_{NN}}$	0–10% Ω^-	3.125 ± 0.037	0.02851 ± 0.00140	0.001
		0–10% $\bar{\Omega}^+$	3.123 ± 0.028	0.02770 ± 0.00105	0.007
		10–20% Ω^-	2.784 ± 0.159	0.03345 ± 0.00536	0.096
		10–20% $\bar{\Omega}^+$	2.915 ± 0.228	0.02717 ± 0.00768	0.184
		20–40% Ω^-	2.613 ± 0.135	0.03600 ± 0.00521	0.179
		20–40% $\bar{\Omega}^+$	2.770 ± 0.173	0.02560 ± 0.00667	0.292
		40–60% Ω^-	2.626 ± 0.086	0.02964 ± 0.00291	0.030
		40–60% $\bar{\Omega}^+$	2.336 ± 0.349	0.03187 ± 0.01177	0.537
			Single Erlang distribution in Fig. 2		
Figure 5(g)	$\langle p_t \rangle - C$	11.5 GeV Ω^-	0.326 ± 0.000	-0.00093 ± 0.00000	0.001
		11.5 GeV $\bar{\Omega}^+$	0.304 ± 0.000	-0.00047 ± 0.00000	0.001
		19.6 GeV Ω^-	0.321 ± 0.006	-0.00052 ± 0.00021	0.075
		19.6 GeV $\bar{\Omega}^+$	0.318 ± 0.001	-0.00056 ± 0.00002	0.001
		27 GeV Ω^-	0.346 ± 0.010	-0.00076 ± 0.00034	0.155
		27 GeV $\bar{\Omega}^+$	0.358 ± 0.008	-0.00139 ± 0.00027	0.153
		39 GeV Ω^-	0.336 ± 0.003	-0.00041 ± 0.00007	0.030
		39 GeV $\bar{\Omega}^+$	0.341 ± 0.003	-0.00051 ± 0.00008	0.030
Figure 5(h)	$\langle p_t \rangle - \sqrt{s_{NN}}$	0–10% Ω^-	0.319 ± 0.010	0.00046 ± 0.00040	0.121
		0–10% $\bar{\Omega}^+$	0.292 ± 0.018	0.00135 ± 0.00067	0.264
		10–20% Ω^-	0.285 ± 0.016	0.00118 ± 0.00056	0.130
		10–20% $\bar{\Omega}^+$	0.294 ± 0.016	0.00108 ± 0.00055	0.116
		20–40% Ω^-	0.273 ± 0.016	0.00175 ± 0.00060	0.271
		20–40% $\bar{\Omega}^+$	0.271 ± 0.010	0.00173 ± 0.00038	0.129
		40–60% Ω^-	0.276 ± 0.002	0.00100 ± 0.00005	0.001
		40–60% $\bar{\Omega}^+$	0.251 ± 0.023	0.00159 ± 0.00077	0.324

Table 6. Values of intercepts, slopes, and χ^2/dof corresponding to the lines in Fig. 6 which shows dependences of parameters on centrality at different energies (a,c,e,g,i) and on energy in different centrality intervals (b,d,f,h,j). The values of parameters are extracted from Fig. 3 and listed in Table 3.

Figure	Relation	Type	Intercept	Slope	χ^2/dof
			Single Tsallis statistics in Fig. 3		
Figure 6(a)	$T - C$	7.7 GeV	0.152 ± 0.001	-0.00005 ± 0.00001	0.001
		11.5 GeV	0.151 ± 0.001	-0.00004 ± 0.00001	0.006
		19.6 GeV	0.154 ± 0.001	-0.00006 ± 0.00001	0.021
		27 GeV	0.153 ± 0.001	0.00003 ± 0.00001	0.005
		39 GeV	0.152 ± 0.001	-0.00002 ± 0.00001	0.012
Figure 6(b)	$T - \sqrt{s_{NN}}$	0–5%	0.152 ± 0.001	-0.00003 ± 0.00004	0.010
		5–10%	0.153 ± 0.002	0.00001 ± 0.00007	0.027
		10–20%	0.150 ± 0.001	0.00010 ± 0.00004	0.014
		20–40%	0.150 ± 0.001	0.00010 ± 0.00006	0.019
		40–60%	0.150 ± 0.002	0.00007 ± 0.00007	0.028
		60–80%	0.148 ± 0.002	0.00012 ± 0.00010	0.055
Figure 6(c)	$q - C$	7.7 GeV	1.026 ± 0.001	-0.00011 ± 0.00002	0.019
		11.5 GeV	1.038 ± 0.001	-0.00017 ± 0.00006	0.322
		19.6 GeV	1.037 ± 0.001	-0.00002 ± 0.00003	0.098
		27 GeV	1.043 ± 0.001	-0.00003 ± 0.00001	0.012
		39 GeV	1.049 ± 0.001	0.00001 ± 0.00001	0.015
Figure 6(d)	$q - \sqrt{s_{NN}}$	0–5%	1.027 ± 0.006	0.00061 ± 0.00024	1.079
		5–10%	1.024 ± 0.002	0.00065 ± 0.00009	0.133
		10–20%	1.022 ± 0.001	0.00071 ± 0.00006	0.053
		20–40%	1.021 ± 0.003	0.00076 ± 0.00014	0.458
		40–60%	1.018 ± 0.003	0.00086 ± 0.00012	0.131
		60–80%	1.014 ± 0.002	0.00093 ± 0.00009	0.120
			Two-component Erlang distribution in Fig. 3		
Figure 6(e)	$k_{E1} - C$	7.7 GeV	0.818 ± 0.001	-0.00023 ± 0.00004	0.017
		11.5 GeV	0.827 ± 0.003	-0.00082 ± 0.00007	0.040
		19.6 GeV	0.831 ± 0.003	-0.00062 ± 0.00008	0.053
		27 GeV	0.873 ± 0.001	-0.00029 ± 0.00003	0.005
		39 GeV	0.917 ± 0.001	-0.00032 ± 0.00004	0.005
Figure 6(f)	$k_{E1} - \sqrt{s_{NN}}$	0–5%	0.787 ± 0.009	0.00325 ± 0.00038	0.128
		5–10%	0.784 ± 0.011	0.00316 ± 0.00045	0.315
		10–20%	0.777 ± 0.012	0.00324 ± 0.00050	0.383
		20–40%	0.762 ± 0.016	0.00354 ± 0.00067	1.138
		40–60%	0.755 ± 0.020	0.00356 ± 0.00082	1.094
		60–80%	0.784 ± 0.020	0.00359 ± 0.00084	1.218
Figure 6(g)	$\langle p_t \rangle_1 - C$	7.7 GeV	0.190 ± 0.001	-0.00020 ± 0.00002	0.009
		11.5 GeV	0.184 ± 0.002	-0.00031 ± 0.00005	0.049
		19.6 GeV	0.191 ± 0.002	-0.00036 ± 0.00005	0.044
		27 GeV	0.210 ± 0.002	-0.00049 ± 0.00005	0.035
		39 GeV	0.226 ± 0.001	-0.00035 ± 0.00003	0.014
Figure 6(h)	$\langle p_t \rangle_1 - \sqrt{s_{NN}}$	0–5%	0.175 ± 0.003	0.00129 ± 0.00014	0.064
		5–10%	0.168 ± 0.006	0.00135 ± 0.00026	0.263
		10–20%	0.170 ± 0.007	0.00112 ± 0.00030	0.349
		20–40%	0.163 ± 0.008	0.00119 ± 0.00032	0.383
		40–60%	0.160 ± 0.008	0.00110 ± 0.00034	0.706
		60–80%	0.158 ± 0.008	0.00092 ± 0.00033	0.517
Figure 6(i)	$\langle p_t \rangle_2 - C$	7.7 GeV	0.241 ± 0.001	-0.00049 ± 0.00004	0.016
		11.5 GeV	0.369 ± 0.007	-0.00069 ± 0.00018	0.393
		19.6 GeV	0.293 ± 0.002	-0.00029 ± 0.00005	0.029
		27 GeV	0.330 ± 0.003	-0.00035 ± 0.00007	0.041
		39 GeV	0.369 ± 0.001	-0.00026 ± 0.00003	0.006
Figure 6(j)	$\langle p_t \rangle_2 - \sqrt{s_{NN}}$	0–5%	0.225 ± 0.010	0.00377 ± 0.00044	0.376
		5–10%	0.208 ± 0.003	0.00416 ± 0.00014	0.029
		10–20%	0.199 ± 0.005	0.00438 ± 0.00019	0.059
		20–40%	0.196 ± 0.006	0.00432 ± 0.00024	0.082
		40–60%	0.187 ± 0.007	0.00452 ± 0.00030	0.156
		60–80%	0.173 ± 0.004	0.00468 ± 0.00018	0.069

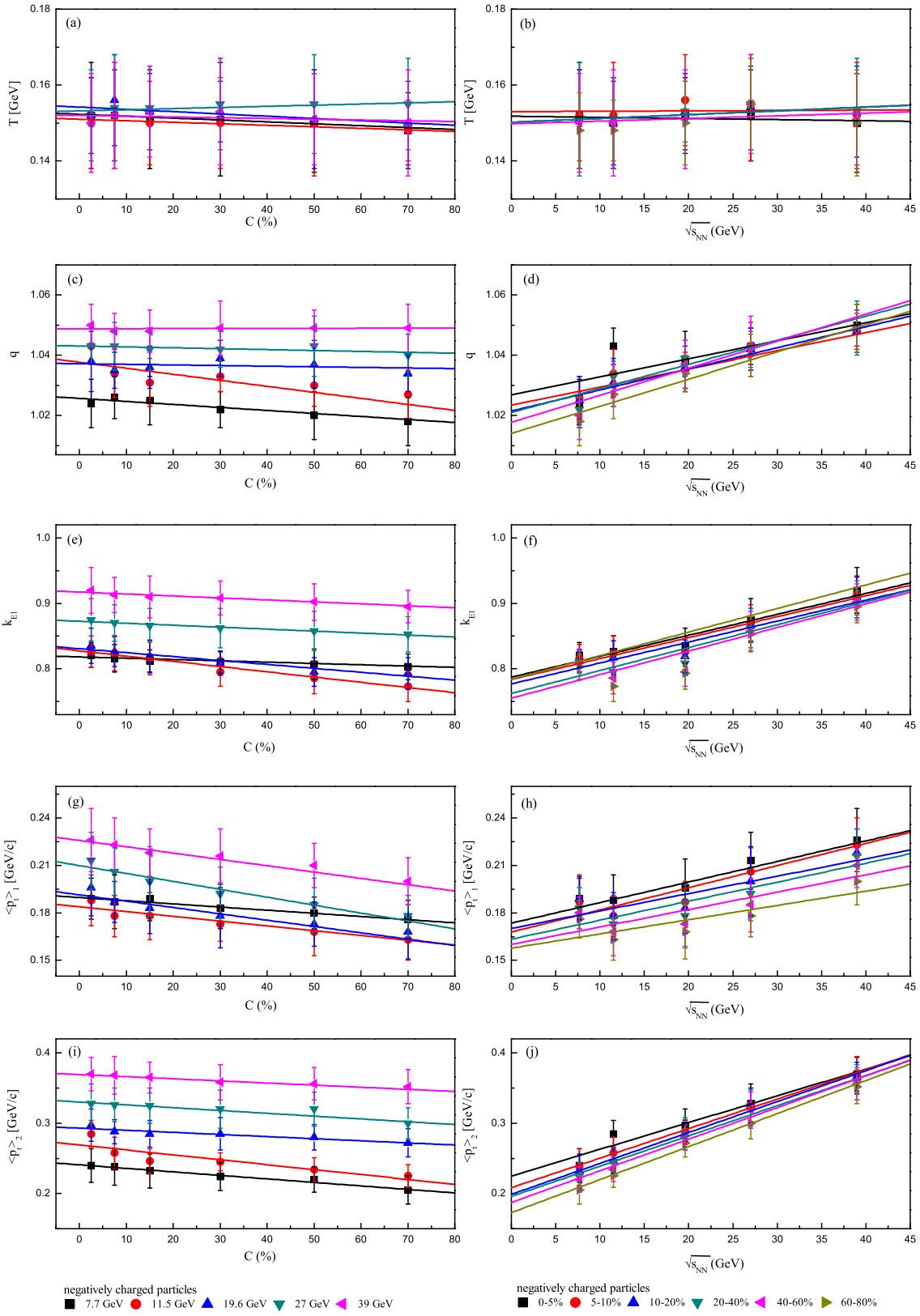

Figure 6. Dependences of parameters (a,b) T, (c,d) q, (e,f) k_{E1}, (g,h) $\langle p_t \rangle_1$, and (i,j) $\langle p_t \rangle_2$ on centrality at different energies (left panel) and on energy in different centrality intervals (right panel). The different symbols represent the parameter values extracted from Fig. 3 and listed in Table 3, where the single Tsallis statistics and two-component Erlang distribution are used for negatively charged particle spectra. The lines are our fitted results.

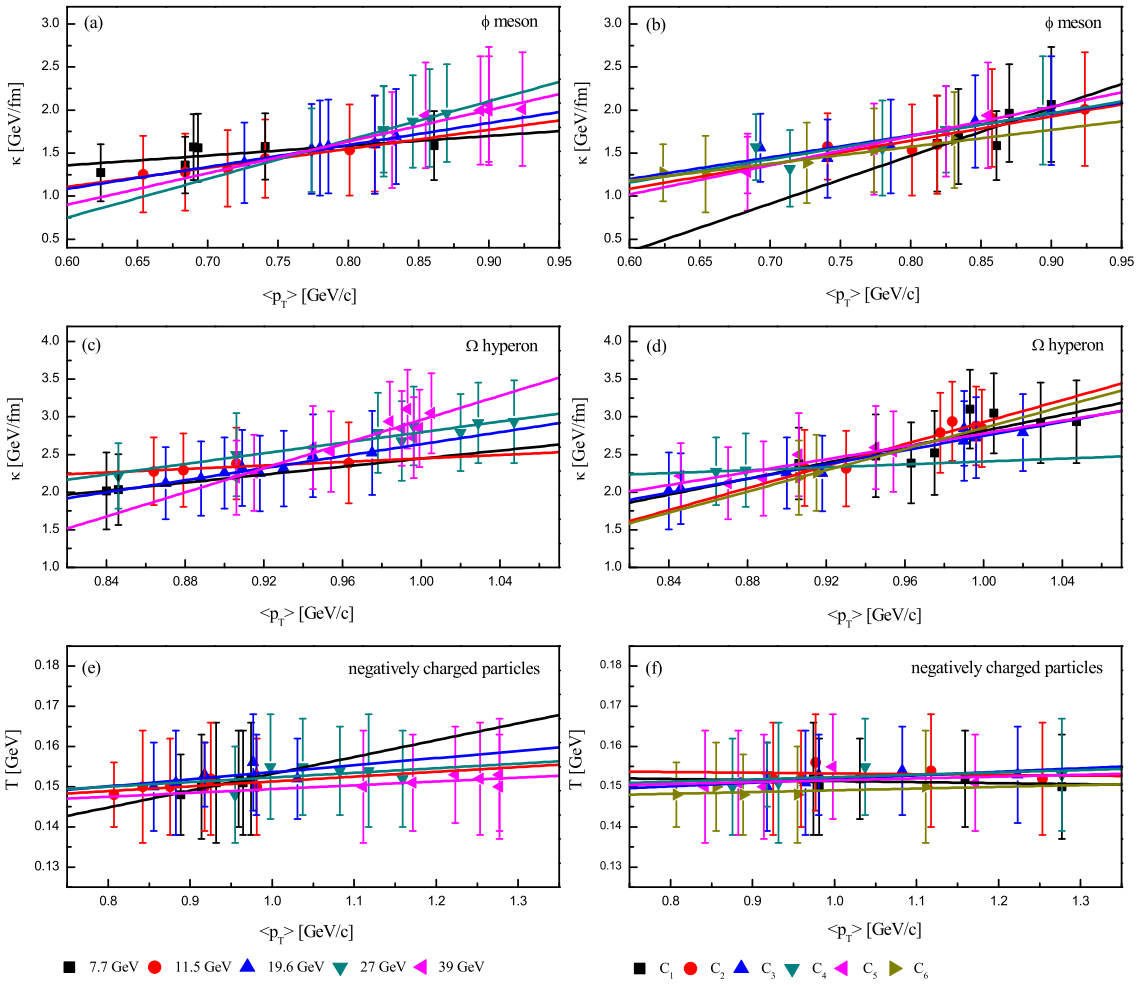

Figure 7. Relations between different parameters, (a,b) κ and $\langle p_T \rangle$ for ϕ mesons, (c,d) κ and $\langle p_T \rangle$ for Ω hyperons, and (e,f) T and $\langle p_T \rangle$ for negatively charged particles. The different symbols represent the parameter values at different energies (in various centrality intervals) (left panel) and in different centrality intervals (at various energies) (right panel), where C_1, C_2, $\cdots$, C_6 for Figures 7(b), 7(d), and 7(f) represent the centrality intervals mentioned in the right panels of Figures 4, 5, and 6, respectively. In some cases the parameter values are obtained by an average weighted by two components which are extracted from Figs. 1–3 and listed in Tables 1–3. The lines are our fitted results.

Table 7. Values of intercepts, slopes, and χ^2/dof corresponding to the lines in Fig. 7 which shows the relations between different parameters.

Figure	Relation	Type	Intercept	Slope	χ^2/dof
Figure 7(a)	$\kappa - \langle p_T \rangle$	7.7 GeV	0.674 ± 0.406	1.139 ± 0.564	0.098
		11.5 GeV	-0.218 ± 0.133	2.208 ± 0.180	0.004
		19.6 GeV	-0.448 ± 0.239	2.553 ± 0.304	0.003
		27 GeV	-1.951 ± 0.092	4.502 ± 0.110	0.001
		39 GeV	-1.305 ± 0.906	3.672 ± 0.024	0.021
Figure 7(b)	$\kappa - \langle p_T \rangle$	0–10%	-2.984 ± 1.712	5.565 ± 1.997	0.117
		10–20%	-0.596 ± 0.628	2.802 ± 0.775	0.057
		20–30%	-0.323 ± 0.502	2.534 ± 0.630	0.072
		30–40%	-0.452 ± 0.575	2.864 ± 0.733	0.111
		40–60%	-1.016 ± 0.262	3.391 ± 0.341	0.020
		60–80%	-0.001 ± 0.153	1.966 ± 0.211	0.011
Figure 7(c)	$\kappa - \langle p_T \rangle$	7.7 GeV	-0.221 ± 0.001	2.666 ± 0.001	0.001
		11.5 GeV	1.274 ± 0.342	1.174 ± 0.379	0.005
		19.6 GeV	-1.353 ± 0.446	3.990 ± 0.486	0.008
		27 GeV	-0.715 ± 0.361	3.511 ± 0.369	0.019
		39 GeV	-5.062 ± 1.010	8.021 ± 1.041	0.052
Figure 7(d)	$\kappa - \langle p_T \rangle$	0–10%	-2.481 ± 1.539	5.294 ± 1.564	0.148
		10–20%	-4.378 ± 0.991	7.308 ± 1.025	0.035
		20–40%	-1.980 ± 0.370	4.726 ± 0.393	0.026
		10–60%	1.447 ± 0.001	0.959 ± 0.001	0.001
		40–60%	-1.496 ± 0.986	4.273 ± 1.093	0.054
		60–80%	-4.203 ± 0.022	7.058 ± 0.025	0.001
Figure 7(e)	$T - \langle p_T \rangle$	7.7 GeV	0.111 ± 0.007	0.042 ± 0.008	0.003
		11.5 GeV	0.139 ± 0.006	0.012 ± 0.007	0.010
		19.6 GeV	0.136 ± 0.011	0.018 ± 0.012	0.031
		27 GeV	0.141 ± 0.016	0.012 ± 0.015	0.054
		39 GeV	0.140 ± 0.010	0.010 ± 0.008	0.011
Figure 7(f)	$T - \langle p_T \rangle$	0–5%	0.154 ± 0.004	-0.003 ± 0.004	0.010
		5–10%	0.155 ± 0.007	-0.002 ± 0.006	0.027
		10–20%	0.143 ± 0.005	0.009 ± 0.005	0.017
		20–40%	0.147 ± 0.005	0.006 ± 0.005	0.029
		40–60%	0.147 ± 0.007	0.005 ± 0.008	0.032
		60–80%	0.145 ± 0.004	0.004 ± 0.004	0.010

References

[1] S. Chatterjee, S. Das, L. Kumar, D. Mishra, B. Mohanty, R. Sahoo, N. Sharma, Adv. High Energy Phys. **2015**, 349013 (2015).

[2] Y. Zhong, C.-B. Yang, X. Cai, S.-Q. Feng, Adv. High Energy Phys. **2015**, 193039 (2015).

[3] J. Uphoff, O. Fochler, Z. Xu, C. Greiner, Acta Phys. Pol. B Proc. Suppl. **5**, 555 (2012).

[4] R. C. Hwa, Adv. High Energy Phys. **2015**, 526908 (2015).

[5] G.-L. Ma, M.-W. Nie, Adv. High Energy Phys. **2015**, 967474 (2015).

[6] D. D. Ivanenko, D. F. Kurdgelaidze, Astrofizika **1**, 479 (1965) [Astrophysics **1**, 251 (1965)].

[7] N. Itoh, Prog. Theor. Phys. **44** 291, (1970).

[8] T. D. Lee, G. C. Wick, Phys. Rev. D **9**, 2291 (1974).

[9] M. Nasim, V. Bairathi, M. K. Sharma, B. Mohanty, A. Bhasin, Adv. High Energy Phys. **2015**, 197930 (2015).

[10] For the STAR Collaboration (L. Kumar), *Talk given the 2011 Meeting of the Division of Particles and Fields of the American Physical Society (DPF 2011), Rhode Island, USA, August 9-13, 2011*, arXiv:1109.5313 (2011).

[11] For the STAR collaboration (S. Das), EPJ Web of Conf. **90**, 08007 (2015).

[12] For the STAR collaboration (S. S. Shi), Acta Phys. Pol. B Proc. Suppl. **5**, 311 (2012).

[13] For the NA49 NA61/SHINE Collaborations (M. Gazdzicki), J. Phys. G **38**, 124024 (2011).

[14] For the NA61/SHINE Collaboration (M. Mackowiak-Pawlowska), PoS (EPS-HEP2015), 205 (2015), arXiv:1510.08688 (2015).

[15] For the NA61 Collaboration (M. Mackowiak), J. Phys. Conf. Ser. **270**, 012048 (2011).

[16] For the NA61/SHINE Collaboration (D. T. Larsen), arXiv:1510.00674 (2015).

[17] For the STAR Collaboration (L. Kumar), J. Phys. G **38**, 124145 (2011).

[18] A. Rustamov, Cen. Eur. J. Phys. **10**, 1267 (2012).

[19] M. Bleicher, arXiv:hep-ph/0509314 (2005).

[20] J. Steinheimer, M. Bleicher, Eur. Phys. J. A **48**, 100 (2012).

[21] Y. B. Ivanov, D. Blaschke, Phys. Rev. C **92** 024916 (2015).

[22] Y. B. Ivanov, *Talk given at the 15th International Conference on Strangeness in Quark Matter (SQM2015), Dubna, Russia, 6-11 July 2015*, arXiv:1509.06944 (2015).

[23] F.-H. Liu, L.-N. Gao, R. A. Lacey, Adv. High Energy Phys. **2016**, 9467194 (2016).

[24] R. A. Lacey, Phys. Rev. Lett. **114**, 142301 (2015).

[25] F.-H. Liu, Y.-Q. Gao, T. Tian, B.-C. Li, Eur. Phys. J. A **50**, 94 (2014).

[26] F.-H. Liu, J.-S. Li, Phys. Rev. C **78**, 044602 (2008).

[27] F.-H. Liu, Nucl. Phys. A **810**, 159 (2008).

[28] J. Schwinger, Phys. Rev. **82**, 664 (1951).

[29] R.-C. Wang, C.-Y. Wong, Phys. Rev. D **38**, 348 (1988).

[30] C.-Y. Wong, *Introduction to High Energy Heavy Ion Collisions*, World Scientific, Singapore, 1994.

[31] P. Braun-Munzinger, K. Redlich, J. Stachel, in *Quark-Gluon Plasma 3*, edited by R. C. Hwa, X.-N. Wang (World Scientific, Singapore, 2004), arXiv:nucl-th/0304013 (2004).

[32] C. Tsallis, J. Stat. Phys. **52**, 479 (1988).

[33] T. S. Biró, G. Purcsel, K. Ürmössy, Eur. Phys. J. A **40**, 325 (2009).

[34] J. Cleymans, D. Worku, Eur. Phys. J. A **48**, 160 (2012).

[35] STAR Collaboration (L. Adamczyk *et al.*), arXiv:1506.07605 (2015).

[36] For the STAR Collaboration (M. V. Tokarev), *Talk given at the International Conference "HADRON STRUCTURE'15", Horny Smokovec, Slovak Republic, 29 June – 3 July, 2015*, arXiv:1509.06570, (2015).

[37] A. Andronic, P. Braun-Munzinger, J. Stachel, Nucl. Phys. A **834**, 237c (2010).

[38] F.-H. Liu, Y.-Q. Gao, H.-R. Wei, Adv. High Energy Phys. **2014**, 293873 (2014).

[39] L.-N. Gao, F.-H. Liu, Adv. High Energy Phys. **2016**, 1505823 (2016).

[40] H.-R. Wei, Y.-H. Chen, L.-N. Gao, F.-H. Liu, Adv. High Energy Phys. **2014**, 782631 (2014).